清华大学学位论文 LaTeX 模板

使用示例文档 v7.3.1

Cryogenic Trapped-Ion System for Multiqubit Quantum Memory

(申请清华大学工学硕士学位论文)

培 养 单 位 ： 计算机科学与技术系

学　　科 ： 计算机科学与技术

研 究 生 ： 薛 瑞 尼

指 导 教 师 ： 郑 纬 民　教 授

副指导教师 ： 陈 文 光　教 授

二〇二三年三月

Cryogenic Trapped-Ion System for Multiqubit Quantum Memory

Thesis submitted to

Tsinghua University

in partial fulfillment of the requirement

for the degree of

Master of Science

in

Computer Science and Technology

by

Xue Ruini

Thesis Supervisor: Professor Zheng Weimin

Associate Supervisor: Professor Chen Wenguang

March, 2023

学位论文指导小组、公开评阅人和答辩委员会名单

指导小组名单

李 1XX	教授	清华大学
王 XX	副教授	清华大学
张 XX	助理教授	清华大学

公开评阅人名单

刘 XX	教授	清华大学
陈 XX	副教授	XXXX 大学
杨 XX	研究员	中国 XXXX 科学院 XXXXXXX 研究所

答辩委员会名单

主席	赵 XX	教授	清华大学
委员	刘 XX	教授	清华大学
	杨 XX	研究员	中国 XXXX 科学院 XXXXXXX 研究所
	黄 XX	教授	XXXX 大学
	周 XX	副教授	XXXX 大学
秘书	吴 XX	助理研究员	清华大学

关于学位论文使用授权的说明

本人完全了解清华大学有关保留、使用学位论文的规定，即：

清华大学拥有在著作权法规定范围内学位论文的使用权，其中包括：（1）已获学位的研究生必须按学校规定提交学位论文，学校可以采用影印、缩印或其他复制手段保存研究生上交的学位论文；（2）为教学和科研目的，学校可以将公开的学位论文作为资料在图书馆、资料室等场所供校内师生阅读，或在校园网上供校内师生浏览部分内容；（3）按照上级教育主管部门督导、抽查等要求，报送相应的学位论文。

本人保证遵守上述规定。

作者签名：_____　　导师签名：_____

日　　期：_____　　日　　期：_____

摘　要

论文的摘要是对论文研究内容和成果的高度概括 21。摘要应对论文所研究的问题及其研究目的进行描述，对研究方法和过程进行简单介绍，对研究成果和所得结论进行概括。摘要应具有独立性和自明性，其内容应包含与论文全文同等量的主要信息。使读者即使不阅读全文，通过摘要就能了解论文的总体内容和主要成果。

论文摘要的书写应力求精确、简明。切忌写成对论文书写内容进行提要的形式，尤其要避免“第 1 章……；第 2 章……；……”这种或类似的陈述方式。

关键词是为了文献标引工作、用以表示全文主要内容信息的单词或术语。关键词不超过 5 个，每个关键词中间用分号分隔。

关键词：关键词 1；关键词 2；关键词 3；关键词 4；关键词 5

ABSTRACT

An abstract of a dissertation is a summary and extraction of research work and contributions. Included in an abstract should be description of research topic and research objective, brief introduction to methodology and research process, and summary of conclusion and contributions of the research. An abstract should be characterized by independence and clarity and carry identical information with the dissertation. It should be such that the general idea and major contributions of the dissertation are conveyed without reading the dissertation.

An abstract should be concise and to the point. It is a misunderstanding to make an abstract an outline of the dissertation and words “the first chapter”, “the second chapter” and the like should be avoided in the abstract.

Keywords are terms used in a dissertation for indexing, reflecting core information of the dissertation. An abstract may contain a maximum of 5 keywords, with semi-colons used in between to separate one another.

Keywords: keyword 1; keyword 2; keyword 3; keyword 4; keyword 5

TABLE OF CONTENTS

LIST OF FIGURES

LIST OF TABLES

LIST OF SYMBOLS AND ACRONYMS

PI	聚酰亚胺
MPI	聚酰亚胺模型化合物，N-苯基邻苯酰亚胺
PBI	聚苯并咪唑
MPBI	聚苯并咪唑模型化合物，N-苯基苯并咪唑
PY	聚吡咙
PMDA-BDA	均苯四酸二酐与联苯四胺合成的聚吡咙薄膜
MPY	聚吡咙模型化合物
As-PPT	聚苯基不对称三嗪
MAsPPT	聚苯基不对称三嗪单模型化合物，3,5,6-三苯基-1,2,4-三嗪
DMAsPPT	聚苯基不对称三嗪双模型化合物（水解实验模型化合物）
S-PPT	聚苯基对称三嗪
MSPPT	聚苯基对称三嗪模型化合物，2,4,6-三苯基-1,3,5-三嗪
PPQ	聚苯基喹噁啉
MPPQ	聚苯基喹噁啉模型化合物，3,4-二苯基苯并二嗪
HMPI	聚酰亚胺模型化合物的质子化产物
HMPY	聚吡咙模型化合物的质子化产物
HMPBI	聚苯并咪唑模型化合物的质子化产物
HMAsPPT	聚苯基不对称三嗪模型化合物的质子化产物
HMSPPT	聚苯基对称三嗪模型化合物的质子化产物
HMPPQ	聚苯基喹噁啉模型化合物的质子化产物
PDT	热分解温度
HPLC	高效液相色谱（High Performance Liquid Chromatography）
HPCE	高效毛细管电泳色谱（High Performance Capillary lectrophoresis）
LC-MS	液相色谱-质谱联用（Liquid chromatography-Mass Spectrum）
TIC	总离子浓度（Total Ion Content）
ab initio	基于第一原理的量子化学计算方法，常称从头算法
DFT	密度泛函理论（Density Functional Theory）
E_a	化学反应的活化能（Activation Energy）
ZPE	零点振动能（Zero Vibration Energy）
PES	势能面（Potential Energy Surface）
TS	过渡态（Transition State）
TST	过渡态理论（Transition State Theory）

$\Delta G^{\neq}$	活化自由能（Activation Free Energy）
κ	传输系数（Transmission Coefficient）
IRC	内禀反应坐标（Intrinsic Reaction Coordinates）
ν_i	虚频（Imaginary Frequency）
ONIOM	分层算法（Our own N-layered Integrated molecular Orbital and molecular Mechanics）
SCF	自洽场（Self-Consistent Field）
SCRF	自洽反应场（Self-Consistent Reaction Field）

CHAPTER 1 INTRODUCTION

研究生学位论文撰写，除表达形式上需要符合一定的格式要求外，内容方面上也要遵循一些共性原则。

通常研究生学位论文只能有一个主题（不能是几块工作拼凑在一起），该主题应针对某学科领域中的一个具体问题展开深入、系统的研究，并得出有价值的研究结论。学位论文的研究主题切忌过大，例如，“中国国有企业改制问题研究” 这样的研究主题过大，因为 “国企改制” 涉及的问题范围太广，很难在一本研究生学位论文中完全研究透彻。

1.1 论文的语言及表述

除国际研究生外，学位论文一律须用汉语书写。学位论文应当用规范汉字进行撰写，除古汉语研究中涉及的古文字和参考文献中引用的外文文献之外，均采用简体汉字撰写。

国际研究生一般应以中文或英文书写学位论文，格式要求同上。论文须用中文封面。

研究生学位论文是学术作品，因此其表述要严谨简明，重点突出，专业常识应简写或不写，做到立论正确、数据可靠、说明透彻、推理严谨、文字凝练、层次分明，避免使用文学性质的或带感情色彩的非学术性语言。

论文中如出现一个非通用性的新名词、新术语或新概念，需随即解释清楚。

CHAPTER 2 ION TRAPPING

2.1 The $^{171}Yb^{+}$ qubit

With a mass factor of 171 and a nuclear spin of 1/2, $^{171}Yb^{+}$ has been selected as the qubit system candidate in our laboratory. In the experiment, we use an RF trap to trap the $^{171}Yb^{+}$ ion. Hyperfine clock states are used to encode the qubit. They are stable against magnetic fluctuations. The two hyperfine states of the $^{2}S_{1/2}$ manifold are encoded as $|\downarrow_z\rangle \equiv |F=0, m_F=0\rangle$ and $|\uparrow_z\rangle \equiv |F=1, m_F=0\rangle$. The $^{2}S_{1/2} \leftrightarrow {}^{2}P_{1/2}$ transition of the $^{171}Yb^{+}$ ion is nearly cyclic, but there are 0.5% of spontaneous emission events that cause the state to decay to $^{2}D_{3/2}$. Consequently, a 935 nm laser is continuously on to repump the state to $^{3}[3/2]_{1/2}$ and subsequently decays back to $^{2}S_{1/2}$ in order to finish the cycle transition. By addressing the transition $^{2}S_{1/2} \leftrightarrow {}^{2}P_{1/2}$ with a 370 nm laser, Doppler cooling, optical pumping, and state detection may be achieved. With the use of acoustic-optic modulator (AOM) and electro-optic modulator (EOM), we put all these operations into practice.

2.1.1 Two-photon ionization

Generating an ion and loading it into a Paul trap is the first step towards a trapped-ion quantum computer. The energy necessary to ionize neutral ytterbium to $^{171}Yb^{+}$ ion is at least a photon with the wavelength below 198.2 nm in the FUV zone, which is hard to produce as a laser. Instead, we adopt a two-photon ionization method to produce $^{171}Yb^{+}$ with a single valance electron through the intermediate level $^{1}P_{1}$. An enriched Ytterbium atomic source can be used to produce neutral atomic flux towards the trap center. Once the flux is ejected into the trap center, a laser at 398.9110 nm illuminates the region to first ionize the atoms to a highly excited state $^{1}P_{1}$ and then another laser with wavelength below 393.1 nm continuously removes the electron, leaving only a valance electron on the atomic orbits.

Two-photon ionization allows for more precise control of isotope choice. The desired atomic source is often enriched, with an abundance as high as 91.7%, the remainder consists of various natural isotopes, such as ^{174}Yb, ^{172}Yb, ^{168}Yb etc. Assume 50 ions in a large-scale trapped-ion quantum computer, and the average number of dark isotopes is 4. Thankfully, the intermediate level 398.91 nm transition exhibits an isotope-shift, which

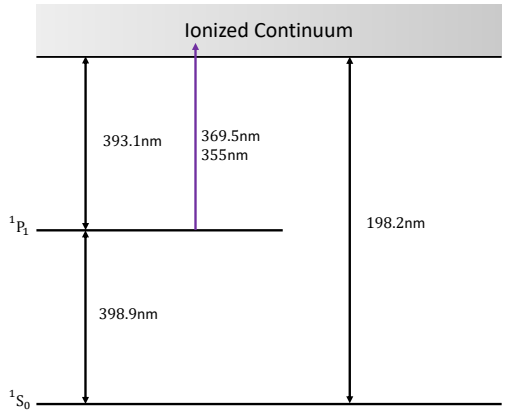

Figure 2.1 Two-photon ionization scheme on $^{171}Yb^+$.

may be used to differentiate between isotopes. Doppler shift is a practical consideration that requires further care. The 398.91 nm laser is oriented perpendicular to the atomic flux to mitigate the Doppler effect. Isotope-selective loading of ions is possible in this setup, increasing the likelihood of the desired isotope, and this may be improved by decreasing the power of the 398.91 nm laser to achieve a narrow linewidth , although this might delay loading speed. Clock states, $\left|\downarrow_z\right\rangle \equiv \left|F=0, m_F=0\right\rangle$ and $\left|\uparrow_z\right\rangle \equiv \left|F=1, m_F=0\right\rangle$, encode the qubit. Doppler cooling, optical pumping and state detection all employ the cyclic transition between the $6^2P_{1/2}$ states and the ground state $6^2S_{1/2}$. A magnetic field applied externally causes a splitting of the $|F=1\rangle$ manifolds through the Zeeman effect at a rate of roughly 1.4 MHz/G, whereas the second-order Zeeman effect dominates the clock qubits at a rate of about 310 Hz/G^2.

Routine ion loading procedures include directing an atomic beam to the loading zone, where several laser beams are utilized to photoionize the atoms. A needle and some shards of metal are all that make up the oven, enriched in 174Yb and 171Yb in separate ovens. On the outside, a current loop is created by connecting the needle's head and tail with Kapton wires to the positive and negative terminals of the power supply. No part of the needle should be anchored to the floor of the chamber. That's because doing so would generate a substantial current to flow into the ground. Since current flows preferentially toward a lower potential, this phenomena may be prevented by isolating the negative poles of the current source from the ground. Keep in mind that while powering the oven for the first time, we must increase the current gradually so as not to accidentally ignite it and safeguard the SAES pump. The first time you use an oven, numerous grimy items will likely be fired out, which might cause the SAES gauge current to rise to the order of A. The atoms are expelled into the trap's central zone after the oven is heated for several

minutes.

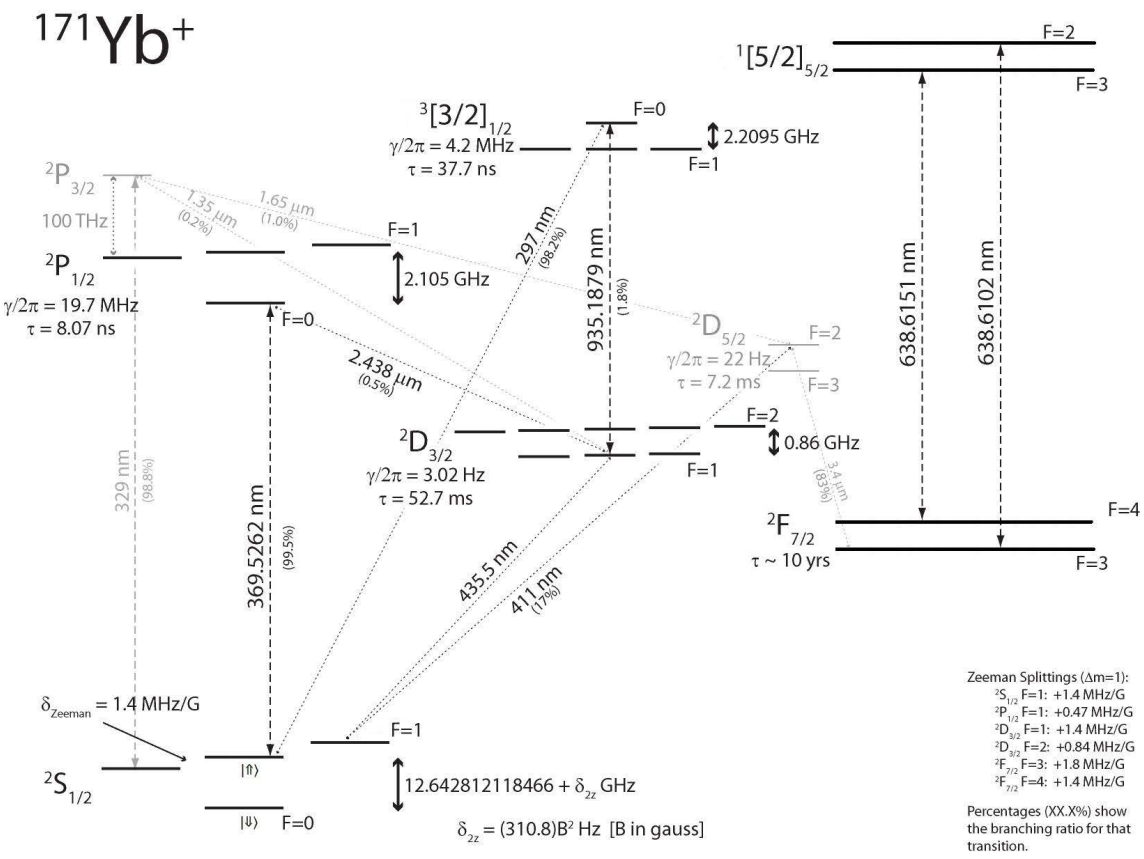

Figure 2.2 $^{171}Yb^{+}$ energy level diagram.

2.1.2 Doppler cooling

Ions have too wide of a motional area to be detected after they have been loaded into the trap since they are still very hot. We must first cool down the heated ions and produce the Coulomb crystal in order to stabilize and crystallize them. Doppler cooling is a method of rapidly cooling ions by utilizing a cyclic transition whose excited state has a very short lifetime and, therefore, a very high cooling rate. Doppler cooling is achieved in the $^{171}Yb^{+}$ system using a red-detuned laser to access $6^2P_{1/2}$ levels with a lifetime of around 8.12 ns, a natural linewidth of 19.6 MHz, and a transition of 369.5263 nm.

Doppler cooling of ions is shown in a simplified model, where ion micromotion is disregarded and the trapping potential is represented by the time-independent pseudo harmonic potential $V(z) = \frac{1}{2}m\omega_z^2 z^2$ just in the z direction. Although the trapped ion's motion is no longer in the quantum domain after Doppler cooling, it can be treated as a classical motion with a velocity that obeys $v(t) = v_0 \cos(\omega_z t)$. Let us consider the hypothetical case of a single, moving laser interacting with a trapped two-level ion consisting only of

S and P states. One cycle of absorption and spontaneous emission occurs in a time period where the ion's velocity does not vary noticeably if the radiative decay rateof the P-level is significantly bigger than the motional frequency. In this scenario, we may represent the average radiation pressure exerted on an ion as a continuous force that varies with its speed. A photon's absorption causes an ion's momentum to increase by $\Delta\mathbf{p} = \hbar\mathbf{k}$ in the direction of the photon's wave vector, and the ion's subsequent spontaneous emission likewise increases its momentum. After many cycles of absorption and emission, the ion will be slowed when the wave vector contains a component along the direction of motion, but the direction of the momentum kick due to spontaneous emission is random across cycles.

The Doppler cooling limit $T_{\min} = \hbar\Gamma(1+\chi)/\left(4k_B\right)$ can be achieved by laser detuning $\Delta = -\frac{\Gamma}{2}$, where χ is the geometrical factor for spontaneous emission, $\Gamma = \sqrt{1+s}\Gamma_0$ is the effective linewidth broadened by power, s is the saturation parameter and the saturation intensity is $I_{\text{sat}} = \frac{\pi hc\Gamma_0}{3\lambda^3} = 510\ \text{W/m}^2$. In addition, re-pumping $|\downarrow\rangle$ back to the cycled transition necessitates an additional frequency component with a detuning of 14.748 GHz. Moreover, the influence of the hyperfine levels must be taken into account, therefore a laser with a wavelength of 935.1880 nm and a sideband of 3.0695 GHz are needed. The branch ratio from level $6^2P_{1/2}$ to level $5^2D_{3/2}$ is non-zero at 0.5%. Doppler cooling may be employed to achieve a final state with a phonon number below 10, where the crystal is stable against certain heating influences from the environment.

2.1.3 Optical pumping

When the ions have been cooled, the $\left|\downarrow_z\right\rangle$ state is prepared using optical pumping. Laser at 370 nm is stimulated when the $^2\,\mathrm{S}_{1/2}\ \mathrm{F} = 1$ to $^2\mathrm{P}_{1/2}\ \mathrm{F} = 1$ transition occurs. If the ion enters the $^2\mathrm{P}_{1/2}\ \mathrm{F} = 1$ manifold, it may spontaneously decay to any of the $^2\,\mathrm{S}_{1/2}$ states. The ion is $\sim$ 10GHz off resonant from the nearest transition. From the $^2\mathrm{P}_{1/2}\ \mathrm{F} = 1$ state, the ion has a 1/3 chance of decaying to the $\left|\downarrow_z\right\rangle$ state. According to the energy diagram, the optical pumping beam has to include both linear and circular components of polarization.

2.1.4 State detection

An experiment's initial step is always preparing the $\left|\downarrow_z\right\rangle$ ion chain. The next step is to actually do the experiment, followed by analysis. When the $\hat{\sigma}_z$ operator is used for measurements, the $|\uparrow\rangle$ and $\left|\downarrow_z\right\rangle$ states of the ions are the only viable results.

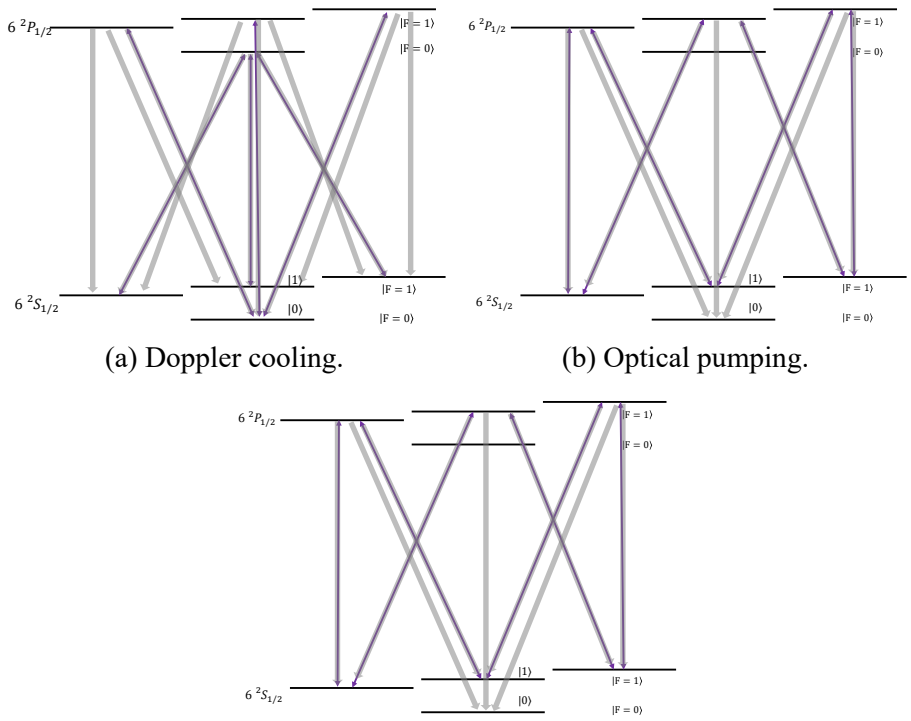

(a) Doppler cooling. (b) Optical pumping.

(c) State detection.

Figure 2.3 The relevant transitions for 369.52 nm laser

It is possible to determine the state of the ion by shining light with a wavelength of 370 nm onto an ion chain that is resonant with the ^{2} $S_{1/2}$ F = 1 to $^2P_{1/2}$ F = 0 transition. This kind of light is known as a detecting light. The detecting light will only resonate with the $|\uparrow\rangle$ state if it is present. It is possible for the ion to decay spontaneously to any of the ^{2} $S_{1/2}$ F = 1 levels. Since it is desirable to have numerous absorption or emission events, the beam has all possible polarization components. This allows the detection process to continue without interruption until sufficient photons have been gathered to determine the ion state. The ion fluoresces isotropically when exposed to the detecting light, and a portion of the light that is emitted by it is gathered by imaging optics and directed onto an EMCCD camera in order to read out the spin state. The detection light has a minuscule chance of off-resonantly exciting either spin state to the $^2P_{1/2}$ F = 1 manifold, where the ion may subsequently decay into the other spin state and induce detection errors. This happens because of the $^2P_{1/2}$ F = 1 manifold.

Doppler cooling, optical pumping, and state detection are all examples of operations that entail spontaneous decay to the ^{2} $S_{1/2}$ F = 1 manifold of states. Hence, if the Zeeman states are degenerate, the mechanism of coherent population trapping may be used to pump the ion into a dark state. As a result, an application of a B-field is made to the ions

in order to disrupt this degeneracy and stop the trapping of coherent populations. In the location where the ions are located, the B-field strength is XX G, and the Zeeman splitting from the $|\uparrow\rangle$ state is measured XX MHz.

We are able to determine the state of the spins in the ion chain by capturing the spin-dependent fluorescence using a site-resolving image Andor IXon Ultra 888 EMCCD camera. During the state detection process, a resonant laser with a wavelength of 370 nm is shone between $|\uparrow\rangle$ and $\left|\downarrow_z\right\rangle$. When the qubit is in the $\left|\downarrow_z\right\rangle$ state, a small amount of photons are scattered off, however when the spin state is in the $|\uparrow\rangle$ state, a significant number of photons are scattered off. The binary threshold for spin-state discrimination is determined by calibrating the number of photons dispersed from the bright $|\uparrow\rangle$ state and the dark $\left|\downarrow_z\right\rangle$ state of each spin at the beginning of the process of collecting data on those spins. The bright and dark states of the setup used in this thesis have an average fidelity of more than 97 %, which is suitable for the quantum memory experiments. The off-resonant mixing of spin states during detection, crosstalk between nearby ions, noise from the electronic camera, and noise from the laser are the primary causes of mistake in this case.

2.2 The linear Paul trap

According to one of Maxwell's equations, $\nabla \cdot \vec{E} = 0$, the electric field will not diverge in a region where there is no free charge density. This conclusion may be drawn from the fact that: Earnshaw deduced from this equation that it was mathematically impossible for a charged particle to be connected in a static electric field in all directions at the same time. Yet, in order to condense charged particles, either oscillating electric fields or a combination of static electric and magnetic fields are required. In this experiment, the RF trap is the primary focus.

Assuming for the sake of this discussion that the ions have a positive charge, mathematically express the criteria of an accessible potential that requires minima in any direction as shown below.

$$\frac{\partial \mathbf{E}}{\partial x_i} = -\frac{\partial^2 \Psi}{\partial x_i^2} < 0, x_i \in \{x, y, z\} \tag{2.1}$$

However, Eq. (2.1) contradicts of the Laplacian equation for static electric fields in vacuum, which states that else there would never be a global minimum in any of the directions otherwise $\frac{\partial \mathbf{E}}{\partial x_i} = 0$

$$\nabla^2 \Psi = 0 \tag{2.2}$$

The ion trap technique, which uses a mix of DC and RF oscillating electric fields, offers a fortunate alternative to the traditional method of confining ions in a vacuum environment. It is possible to write down the broad potential of a Paul trap as

$$\Psi(x, y, z) = \frac{U}{2}\left(\alpha x^2 + \beta y^2 + \gamma z^2\right) + \frac{V}{2}\cos(\Omega t)\left(\alpha' x^2 + \beta' y^2 + \gamma' z^2\right) \tag{2.3}$$

$\alpha, \beta, \gamma, \alpha', \beta', \gamma'$ are geometrical factors. A potential of this kind may be generated using hyperbolic electrodes, the geometrical factors involved are precisely $1/r^2$, where r denotes the distance to the electrodes. Unfortunately, the hyperbolic electrodes restrict the optical access. There are some novel designs for traps with high optical access, but the geometrical considerations need to take into account the approximations that are necessary since the hyperbolic electrodes are not ideal. There is an extra restriction for the geometrical factors that must be satisfied in order to satisfy the Laplacian equation

$$\alpha + \beta + \gamma = 0, \quad \alpha' + \beta' + \gamma' = 0 \tag{2.4}$$

To be more specific, a Paul trap with the parameters $\gamma' = 0, \alpha = \beta = -\frac{\gamma}{2}, \alpha' = -\beta'$ is referred to as a linear trap. In a linear trap, charged particles are only confined by a static field in one direction, while RF fields are used to confine them in the other two directions.

2.2.1 Mathieu equation

With a Paul trap, it is possible to decouple the motion of charged particles in three different directions. In this case, we will treat in x for the sake of simplicity following,

$$m\frac{\mathrm{d}^2 x}{\mathrm{d}t^2} = -Q\left(\alpha U x + \alpha' V \cos(\Omega t) x\right) \tag{2.5}$$

substitute $\tau = \frac{\Omega t}{2}, a_x = \frac{4QU\alpha}{m\Omega^2}, q_x = \frac{2QV\alpha'}{m\Omega^2}$, Eq. (2.5) can be simplified as a Mathieu equation

$$\frac{\mathrm{d}^2 x}{\mathrm{d}\tau^2} + \left(a_x x - 2q_x \cos(2\tau) x\right) = 0 \tag{2.6}$$

In this case, the solution of the lowest order is shown together with the assumptions

that $\left|a_x\right|, q_x^2 \ll 1$,

$$\beta_x = \sqrt{a_x + \frac{q_x^2}{2}}, \quad x(t) = 2AC_0 \cos\left(\beta_x \frac{\Omega t}{2}\right)\left[1 - \frac{q_x}{2}\cos(\Omega t)\right] \tag{2.7}$$

This is a bounded solution with periodic frequency $\omega_x = \frac{\beta_x \Omega}{2}$, which is often referred to as secular motion. The second component in frequency $\Omega \pm \omega_x$ represents the intrinsic micromotion that is induced by the RF fields.

In a further approximation, it is possible to construct an effective time-independent potential to describe the dynamics of charged particles in an RF Paul trap. An example in x is presented below, and we assume that the charge is equal to e.

$$E(x,t) = E_0(x)\cos(\Omega t) \tag{2.8}$$

$$F(x,t) = m\ddot{x} = eE_0(x)\cos(\Omega t) \tag{2.9}$$

where $E_0(x)$ is independent of the time-varying potential and solely depends on positional information. Imagine a crystal that has been stabilized such that all of its ions remain in close proximity to their positions of equilibrium. The only new vibrations that occur are those that are caused by the RF fields.

$$x = x_0 - \frac{eE_0(x_0)}{m\Omega^2}\cos(\Omega t) \tag{2.10}$$

This is the first-order solution to the motion, and we may do additional Taylor expansion at the equilibrium location x_0 to the electric field as well, although this is not necessary.

$$\begin{aligned} E_0(x) &= E_0\left(x_0\right) + \left.\frac{\partial E_0(x)}{\partial x}\right|_{x_0}\left(x - x_0\right) \\ &= E_0\left(x_0\right) - \left.\frac{\partial E_0(x)}{\partial x}\right|_{x_0}\left(\frac{eE_0\left(x_0\right)}{m\Omega^2}\cos(\Omega t)\right) \\ &= E_0\left(x_0\right) - \left.\frac{e}{2m\Omega^2}\frac{\partial E_0^2(x)}{\partial x}\right|_{x_0}\cos(\Omega t) \end{aligned} \tag{2.11}$$

$$\begin{aligned} F(x,t) = m\ddot{x} &= eE_0\left(x_0\right)\cos(\Omega t) - \frac{e^2}{2m\Omega^2}\frac{\partial E_0^2(x)}{\partial x}\bigg|_{x_0}\cos^2(\Omega t) \\ &= eE_0\left(x_0\right)\cos(\Omega t) - \frac{e^2}{2m\Omega^2}\frac{\partial E_0^2(x)}{\partial x}\bigg|_{x_0}(1+\cos(2\Omega t))/2 \end{aligned} \tag{2.12}$$

Assess the influence on average, excluding out the variables that are rapidly fluctuating,

$$\bar{F}(x) = -\frac{e^2}{4m\Omega^2}\frac{\partial E_0^2(x)}{\partial x}\bigg|_{x_0} \tag{2.13}$$

where $E_0(x) = -\alpha' V x$ for the general potential, it is a harmonic confinement that does not rely on whether the ions are positively or negatively charged, and it controls the secular motion of ions inside the trap. Additional words include the source of micromotion, which has an oscillation that is much more rapid and is defined by frequency Ω. Hence, one way to define the pseudo potential is as follows,

$$\Psi_{ps} = \frac{e}{4m\Omega^2}E_0^2(x) = \frac{e\alpha'^2V^2}{4m\Omega^2}x^2 \tag{2.14}$$

This re-creates the conclusion that Earnshaw's theorem came to. It is a valid approximation for equilibrium positions and secular motion of charged particles in an RF trap, and it can be used to calculate the principal axes taking both DC and RF fields into account. The secular frequency is $\omega_x = \frac{e\alpha' V}{\sqrt{2}m\Omega}$, which is consistent with the Mathieu equation. The static confinement can also be taken into account, which is also a harmonic term.

2.2.2 Normal modes

Since the normal modes are entirely decoupled from all directions, particularly the transverse modes that we are working on, we employ a chain of trapped $^{171}Yb^{+}$ ions as the quantum memory in a linear Paul trap. This allows us to study the transverse modes. It is necessary for the trap frequencies to adhere to the relation Eq. (2.15) if the Coulomb crystal is to be contained inside a linear chain.

$$\left(\frac{\omega_r}{\omega_z}\right)^2 \geq \frac{N^{1.73}}{2.53} \tag{2.15}$$

where N is the number of ions, ω_r refers to either the transverse mode ω_x or ω_y, and

ω_z refers to the axial mode with DC confinement.

Instead of using the straightforward Mathieu equation, one needs take into consideration the Coulomb interaction that occurs between the ions when there are a greater number of ions fed into the trap. Both the externally imposed pseudo potential and the Coulomb interactions that occur between the ions work together to decide the shape of the ion crystal.

The inter-ion spacings would not be uniform under a harmonic potential similar to Eq. (2.3), where spacings at the center of an ion chain would be much more tight but loose at the edge. This would require much higher RF potential or lower DC potential to satisfy Eq. (2.15), or else there would be an unstable transition to zigzag mode. Here, we consider N ions in In order to solve the issue, quartic potential is required. This is because increasing the number of electrodes along the z-axis will bring the inter-ion spacings closer to being uniform. As the micromotion is negligible in comparison to the secular motion and all of the ions are aligned with the RF null in the required configuration, the property of the ion crystal may be obtained using the pseudo potential while ignoring the time-dependent RF potential.

The potential in its broadest sense may be expressed as

$$U = \sum_i \left(\frac{\alpha}{2} z_i^2 + \frac{\beta}{4} z_i^4 \right) + \sum_{i<j} \frac{e^2}{4\pi\epsilon_0 \left| z_i - z_j \right|} \tag{2.16}$$

Here, we will define the length unit known as $l = \left(e^2 / 4\pi\epsilon_0 \alpha \right)^{1/3}$, and after that, we will be able to rewrite the potential $u_i \equiv z_i / l$ using dimensionless coordinates and dimensionless energy $U' \equiv 4\pi\epsilon_0 l U / e^2$, respectively.

$$U' = \sum_i \left(\frac{1}{2} u_i^2 + \frac{\beta l^2}{4\alpha} u_i^4 \right) + \sum_{i \neq j} \frac{\mathrm{sgn}(\alpha)}{2 \left| u_i - u_j \right|} \tag{2.17}$$

When we have ascertained the total number of ions and the potential configuration $\frac{\beta l^2}{\alpha}$, we will be able to locate the equilibrium locations by minimizing the energy required to do so. Instead, we might try to solve the gradient equations when the system is at equilibrium.

$$0 = \frac{\partial U'}{\partial u_i} = u_i + \frac{\beta l^2}{\alpha} u_i^3 - \mathrm{sgn}(\alpha) \sum_{i \neq j} \frac{u_i - u_j}{\left| u_i - u_j \right|^3} \tag{2.18}$$

We can further reduce the problem to find the solutions of the gradient equations, which is something that can be easily accomplished by some built-in functions of Wolfram Mathematica such as FindRoot or NSolve. As an alternative to performing the optimization with multiple variables, we can use this method.

When the equilibrium locations have been determined, the Hessian matrix may be used to calculate the axial motional modes

$$\frac{\partial^2 U'}{\partial u_i \partial u_j} = \begin{cases} 1 + \frac{3\beta l^2}{\alpha} u_i^2 + \sum_{k \neq i} \frac{2\,\mathrm{sgn}(\alpha)}{\left|u_i - u_k\right|^3}, & i = j \\ -\frac{2\,\mathrm{sgn}(\alpha)}{\left|u_i - u_j\right|^3}, & i \neq j \end{cases} \tag{2.19}$$

Things would turn out differently with regard to the transverse modes. The COM mode has the maximum frequency, and its bandwidth is quite close to that of the axial COM mode; hence, the transverse modes have a significantly higher population density. Moreover, we are able to include the transverse words into the general form.

$$U = \sum_i \left(\frac{\alpha}{2} z_i^2 + \frac{\beta}{4} z_i^4 + \frac{1}{2} m\omega_x^2 x_i^2 + \frac{1}{2} m\omega_y^2 y_i^2 \right) + \sum_{i<j} \frac{e^2}{4\pi\epsilon_0 \left|\mathbf{r_i} - \mathbf{r_j}\right|} \tag{2.20}$$

For a linear chain configuration, the equilibrium positions for transverse x, y are quite clear that $x_0 = 0$, $y_0 = 0$, and we can use the same dimensionless unit l to simplify the potential expression using notation $uz = z/l$, $ux = x/l$, $uy = y/l$,

The equilibrium positions for transverse x and y in a linear chain configuration are quite obvious: $x_0 = 0$, $y_0 = 0$. We can use the same dimensionless unit, l, to simplify the potential expression by notating it as follows: $uz = z/l$, $ux = x/l$, $uy = y/l$. For a linear chain configuration, the equilibrium positions for transverse x and y are quite obvious.

$$\begin{aligned} U' &= \sum_i \left(\frac{1}{2} uz_i^2 + \frac{\beta l^2}{4\alpha} uz_i^4 + \frac{m\omega_x^2}{2\alpha} ux_i^2 + \frac{m\omega_y^2}{2\alpha} uy_i^2 \right) + \sum_{i \neq j} \frac{\mathrm{sgn}(\alpha)}{2\left|\mathbf{u_i} - \mathbf{u_j}\right|} \\ &= U_0 + \sum_i \left(\frac{m\omega_x^2}{2\alpha} ux_i^2 + \frac{m\omega_y^2}{2\alpha} uy_i^2 \right) - \mathrm{sgn}(\alpha) \sum_{i \neq j} \frac{\left(ux_i - ux_j\right)^2 + \left(uy_i - uy_j\right)^2}{4\left|uz_i - uz_j\right|^3} \end{aligned} \tag{2.21}$$

where U_0 is the one only related to coordinates uz_i's. When thinking about the transverse modes, we don't need to take them into account at all since we may ignore them. We may also derive the Hessian matrix for x, y, and the results for x are shown below. As the right hand side of the potential has the same dependency on the sign of α, we can,

in practice, use the absolute value instead.

$$\frac{\partial^2 U'}{\partial u x_i \partial u x_j} = \begin{cases} \frac{m\omega_x^2}{|\alpha|} - \sum_{k \neq i} \frac{1}{\left|uz_i - uz_k\right|^3}, & i = j \\ \frac{1}{\left|uz_i - uz_j\right|^3}, & i \neq j \end{cases} \tag{2.22}$$

2.2.3 Micromotion minimization

Ions in Paul's tarp will go through a process known as forced motion, which is driven by the frequency referred to as Ω. Some of this motion is an intrinsic effect caused by the RF potential, while other motion is caused by forced motion for ions going through a process known as nonzero oscillating force. The force may be created by a residual DC field that moves the ions away from the RF null, and the real-time electric field is not zero. The temporal dependency of the real-time electric field's frequency is characterized by Ω. The motion of ions may, as a matter of course, be explained by the linear superposition of two portions.

$$\begin{aligned} \ddot{x} &= -\omega_x^2 x - \frac{E_0\left(x_0\right) e}{m} \cos(\Omega t) \\ x(t) &= A \cos\left(\omega_x t\right) + B\left(E_0\left(x_0\right)\right) \cos(\Omega t) \end{aligned} \tag{2.23}$$

The periodic force will cause the second term of the solution of $x(t)$, which is given by pseudo potential approximation. The term $B(E_0(x_0))$ is the amplitude of excess micromotion, and it dependends on the strength of the residual electric field $E_0(x_0)$ or the equilibrium position from RF null x_0. In addition, the intrinsic micromotion that is solved by the Mathieu equation is characterized by the frequency $\Omega \pm \omega_x$, and it is related to the transverse secular motion. On the other hand, the excess micromotion are detached from the secular motion. In addition, excess micromotion is degenerate in three directions, and in order to link the micromotion, we require a number of lasers that are not parallel to one another.

In addition to the equation that is described in Eq. (2.23), we are able to utilize the Mathieu equation to determine the motion of the ions in the presence of a stray field, and this motion may be written as

$$\begin{aligned} x(t) &= \left(\frac{eE_R}{m\omega_x^2} + A\cos\left(\omega_x t\right)\right)\left(1 + \frac{q_x}{2}\cos(\Omega t)\right) \\ &= A\cos\left(\omega_x t\right) + \frac{eE_R q_x}{2m\omega_x^2}\cos(\Omega t) + \frac{Aq_x}{2}\cos\left(\omega_x t\right)\cos(\Omega t) + \frac{eE_R}{m\omega_x^2} \end{aligned} \tag{2.24}$$

As can be seen in the figure referenced above, there are four different terms: secular motion, excess micromotion, intrinsic micromotion, and equilibrium position displacement, respectively. Because intrinsic micromotion is born with the RF potential, its amplitude can never be reduced by tinkering with the DC configurations. This is because intrinsic micromotion is only related to the RF potential and the Doppler cooling limit. For secular motion, the amplitude is related to the process of cooling, and $\omega_x = \sqrt{a_x + \frac{q_x^2}{2}}\frac{\Omega}{2}$ for the intrinsic micromotion. It is obvious that the excess micromoiton is associated with the stray field that is exerted on the ions, the amplitude is proportional to $a_x << q_x^2$, in particular for transverse modes in an ion chain, and it can be easily demonstrated that the amplitude will be reduced when increasing the RF level, and in addition to this, the ion position will approach the RF null by factor $\frac{1}{a_x + \frac{q_x^2}{2}}$.

Expanding the electric field is possible within the context of the rotating frame of the ions' secular motion,

$$E(x,t) = E_0 e^{-i\left(\omega_0 t - k_x x(t)\right)} = E_0 e^{ik_x A\cos\left(\omega_x t\right)\left(1+\frac{q_x}{2}\cos(\Omega t)\right)} e^{-i\left(\omega_0 t - \frac{k_x eE_R q_x}{2m\omega_x^2}\cos(\Omega t)\right)} \tag{2.25}$$

So, we are able to make use of the modulation information in order to extract the amplitude of excess micromotion, and the RF modulation may also regulate the fluorescence. A cooling laser is used in this technique to detect the modulation, and of course, non-parallel lasers are required in order to reconstruct the full information of excess micromotion. The fluorescence can be demodulated by using a device called a time-arrival-converter, but this method has some drawbacks. Unfortunately, because of the geometry of the chamber, it is not always possible to send lasers in all three directions, and this difficulty might be considerably more severe for surface planar traps, particularly when the cooling laser is operating in the ultraviolet range. A combination of Raman sideband and EMCCD monitoring ion position is another method that may be used to identify excess micromotion.

In this article, we present the parametric excitation approach for the purpose of min-

imizing excess micromotion because of its ease of use and high degree of accuracy. Although the delivery of laser along the objective might be challenging, the accuracy of micromotion minimization along the objective is completely constrained by the resolution and amplification capabilities of the imaging system. This was covered in the previous section. To be able to detect extra micromotion in any of the three orthogonal directions, parametric excitation just needs a single cooling beam to readily connect to all three directions simultaneously. It is possible to put it into practice by modulating the amplitude of RF fields, using the pseudo potential approximation, the force that is exerted on the ions is

$$\frac{\mathrm{d}^2\bar{x}}{\mathrm{d}t^2} + \xi\frac{\mathrm{d}\bar{x}}{\mathrm{d}t}\omega_x^2\left(1 + 2h\cos\left(\omega_m t\right)\right)\bar{x} = \frac{eE_R}{m} \tag{2.26}$$

where h is the modulation index, $E(r,t) = E_0(r,t)(1 + h\cos(\omega_m t))$, the corresponding pseudo potential is proportional to $E^2(r,t) = E_0^2(r,t)(1 + 2h\cos(\omega_m t))$, and ξ is the damping coefficient of the cooling beam.

The parametric excitation, in contrast to the forced oscillation, will not take place if the initial condition $\bar{x}(0) = 0$, and the parametric excitation will only be excited at the modulation frequency $\omega_m = \frac{2\omega_x}{n}$, where n is a positive integer. The forced oscillation will take place regardless of the initial condition. Depending on the experimental regime, the parametric excitation will either induce a decrease in fluorescence or an increase in it. So, the parametric excitation may be utilized to identify excess micromotion if ions are pushed away from the RF null. Nevertheless, once $\bar{x}$ approaches the equilibrium location of the RF null, the parametric excitation will cease to exist.

In addition, a recent piece of research demonstrates that there is a link between the fluorescence and the amplitude modulation signal. In this example, we will show how parametric excitation may occur when $\omega_m = \omega_x$. The stable solution may be derived by using Floquet theory even in the absence of explicit derivations, which take into account corrections for secular frequency and modulation depth.

$$\bar{x}(t) = \sum_n c_n e^{ic_n\omega_m t} \tag{2.27}$$

$c_n = c_{-n}^*$ for symmetry, and c_0 depends on the first order of modulation, $c_0 = \frac{eE_R}{m\omega_x^2}$.

Then we can extend it to the second order, and we can simplify $\bar{x}(t) = c_0 + 2\mathfrak{R}\left(c_{-1}e^{-i\omega_m t}\right)$, replace it back into Eq. 2.26, and we can easily find the answer for the

second order,

$$\left\|c_{-1}\right\|^2 = \frac{2c_0^2h^2}{\left(f^2-1\right)+4f^2d^2}, \quad \tan\left(\arg\left(c_{-1}\right)\right) = \frac{2fd}{f^2-1} \tag{2.28}$$

where $f = \frac{\omega_m}{\omega_x}$, $d = \frac{\xi}{\omega_x}$ are normalized frequency and damping factor. The amplitude of c_{-1} is linearly proportional to c_0, and thus E_R.

By scanning the modulation frequency across ω_x, which indicates the resonant frequency, it is obvious that there is a phase shift of π. This phase shift may be aided further by the peak value of c_{-1} that occurs during a frequency scan. The sensitivity is influenced by two factors: (a) the modulation factor h, and (b) the degree to which the modulation frequency is detuned with respect to the secular frequency. Notice that there is a correction to the secular frequency that is related to the modulation, but that it is not represented here. The fundamental physics, however, remains the same.

2.3 Coherent manipulation of ions

The $^{171}Yb^+$ qubits are the primary research topic in our laboratory, the qubit itself is encoded in the ground state manifold's two hyperfine levels. In order to manipulate the qubit using a laser, one must make use of the Raman transition, which is facilitated by various auxiliary energy levels.

2.3.1 Theory of laser-ion interaction

In this part, I will focus on the interaction of a single ion with the laser. The application of this concept to the situation of several ions is quite simple, with the exception of the laborious indexing required for the normal mode ladder operators. The Halmitonian for the trapped ion that was irradiated by the laser is as follows: $\hat{H} = \hat{H}_0 + \hat{V}$, where $\hat{H}_0$ refers to the non-interacting component and $\hat{V}$ refers to the interaction part. After being cooled by Doppler cooling, it is possible to safely view it as a harmonic oscillator, even if there is just a single ion trapped in the potential. And if we are just concerned with a two-level internal system and a z-axis exterior motion of the ion, then (we shall set $\hbar$ as 1 in the following) $\hat{H}_0 = \omega_0/2\hat{\sigma}_z + \nu\hat{a}^\dagger\hat{a}$, where ω_0 operator for the annihilation of the z-axis motion. We now deduce the laser-ion interaction, denoted by the symbol $\hat{V}$; however, we only take into account the electric-field component of the laser and use a semi-classical point of view, this means that the laser field is not quantized,

$$\mathbf{E} = \frac{\mathbf{E}_0}{2}\left(e^{i\left(\omega_L t - \mathbf{k}\cdot\mathbf{R} + \varphi_L\right)} + e^{-i\left(\omega_L t - \mathbf{k}\cdot\mathbf{R} + \varphi_L\right)}\right), \tag{2.29}$$

where $\mathbf{R}$ represents the position vector of the ion, $\mathbf{E}_0$ represents the amplitude of the laser field, ω_L represents the frequency of the laser field, and φ_L represents the phase of the laser field. In this context, we will use the example of dipole interaction. The location of the ion along the z axis may be expanded by the ladder operator, $\hat{z} = \bar{z} + z_0(\hat{a}^\dagger + \hat{a})$, where $\bar{z}$ is the average position, z_0 is the motional extent, and $\hat{a}\,(\hat{a}^\dagger)$ was just described above. The motional extent is the distance traveled by the ion along the z axis. The dipole interaction Hamiltonian might therefore be written as

$$\hat{V} = -e\left(\mathbf{r}_{eg}\hat{\sigma}_+ + \mathbf{r}_{eg}\hat{\sigma}_-\right)\cdot\frac{\mathbf{E}_0}{2}\left(e^{i\left(\omega_L t - \eta\left(\hat{a}^\dagger + \hat{a}\right) + \phi\right)} + \text{ H.c. }\right), \tag{2.30}$$

where $\mathbf{r}_{eg} = \langle e|\hat{\mathbf{r}}|g\rangle, \hat{\sigma}_+\left(\hat{\sigma}_-\right)$is $|e\rangle\langle g|(|g\rangle\langle e|), \eta = z_0 k\cos\theta$ is a parameter derived from the Lamb-Dicke equation that describes the relationship between the ion-motional extent and the laser wavelength. This parameter is often considerably less than 1, and in our configuration, it is between $0.07 - 0.09$ away from a transverse mode. And $\phi = \varphi_L - k\cos\theta\bar{z}$ is just a re-defined laser phase factor. In the formulas that have come before, the symbol θ refers to the angle that exists between the laser wave vector $\mathbf{k}$ and the ion-motional axis z. We put the whole Hamiltonian into the interaction picture of the uncoupled Hamiltonian, $\hat{H}_0$ with $\hat{U}_0 = e^{i\hat{H}_0 t}$,

$$\begin{aligned}\hat{H}_I &= \hat{U}_0\hat{H}\hat{U}_0^\dagger - i\hat{U}_0\frac{\partial\hat{U}_0^\dagger}{\partial t}\\ &= -e\left(\mathbf{r}_{eg}\hat{\sigma}_+ e^{i\omega_0 t} + \mathbf{r}_{eg}\hat{\sigma}_- e^{-i\omega_0 t}\right)\cdot\frac{\mathbf{E}_0}{2}\left(e^{i\left(\omega_L t - \eta\left(\hat{a}^\dagger e^{i\nu t} + \hat{a}e^{-i\nu t}\right) + \phi\right)} + \text{ H.c. }\right)\end{aligned} \tag{2.31}$$

By using the rotating wave approximation, we are able to eliminate the high frequency components, which are on the order of $\omega_L + \omega_0$, and get the Hamiltonian that is associated with the interaction picture,

$$\hat{H}_I = -e\mathbf{r}_{eg}\cdot\frac{\mathbf{E}_0}{2}\hat{\sigma}_+ e^{-i(\delta t + \phi)}e^{i\eta\left(\hat{a}^\dagger e^{i\nu t} + \hat{a}e^{-i\nu t}\right)} + H.c. \tag{2.32}$$

where $\delta = \omega_L - \omega_0$ is the detuning. We decided to go with $\Omega = -e\mathbf{r}_{eg}\cdot\mathbf{E}_0 e^{-i\phi}$, which is known as the Rabi frequency, then the $\hat{H}_I$ is

$$\hat{H}_I = \frac{\Omega}{2}\hat{\sigma}_+ e^{-i\delta t} e^{i\eta\left(\hat{a}^\dagger e^{i\nu t} + \hat{a}e^{-i\nu t}\right)} + \text{ H.c.} \tag{2.33}$$

We make the observation that this Hamiltonian is generated from the dipole interaction, nevertheless, for any other sort of interactions, whether quadrupole or Raman interaction, the Hamiltonian of laser and ion is always of the same form. The only thing that is different is the concrete representation of the Rabi frequency, which is denoted by Ω, but we are not too concerned about it since it can be determined by experimentation. As the ytterbium hyperfine qubits are the primary research topic in our laboratory, I will provide an in-depth depiction of the Raman interaction in the next part.

Let us proceed by assuming the following form for the detuning δ of the laser frequency ω_L from the atomic frequency ω_0,

$$\delta = \omega_L - \omega_0 = k\nu,\ k = 0, \pm 1, \pm 2, \ldots \tag{2.34}$$

We apply BCH theorem ① to equation (2.33),

$$\hat{H}_I = \frac{\Omega}{2}\hat{\sigma}_+ e^{-\eta^2/2} \sum_{n,m=0}^{\infty} (i\eta)^{n+m} \frac{(a^\dagger)^n}{n!}\frac{a^m}{m!} e^{i\nu t(n-m-k)} + H.c. \tag{2.35}$$

If the laser is tuned at the frequency ω_L such that $k = 0$, the spectral line is called the carrier. For $k > 0$ ($k < 0$), the spectral line is termed the kth blue (red) sideband because the laser is blue (red) detuned from the atomic frequency ω_0.

The spectral line is referred to as the carrier when the laser is adjusted to operate at the frequency ω_L in such a way that $k = 0$. Since the laser is blue (or red) detuned from the atomic frequency ω_0, the spectral line is referred to as the kth blue (or red) sideband when $k > 0$ (or $k < 0$), respectively.

As a result, the Hamiltonian of the kth order, denoted by the symbol $\hat{H}_I^k$, may be written as follows,

for $k > 0$

$$\hat{H}_I^k = \sum_{m=0}^{\infty} \left(\frac{\Omega_{m,m+k}}{2} |e\rangle\langle g| \otimes |m+k\rangle\langle m| + \text{ H.c.} \right), \tag{2.36}$$

for $k < 0$

① $e^X e^Y = e^Z$ where $Z = X + Y + \frac{1}{2}[X,Y] + \frac{1}{12}[X,[X,Y]] - \frac{1}{12}[Y,[X,Y]] + \cdots$

$$\hat{H}_I^k = \sum_{m=0}^{\infty} \left(\frac{\Omega_{m,m+|k|}}{2} |e\rangle\langle g| \otimes |m\rangle\langle m+|k|| + H.c. \right), \tag{2.37}$$

where for $k > 0$, $\Omega_{m,m+k} = \Omega_{m+k,m} = \Omega e^{-\eta^2/2} (i\eta)^k L_m^k(\eta^2) \sqrt{\frac{m!}{(m+k)!}}$ is the Rabi frequency between the two states, $|g\rangle|m\rangle(|g\rangle|m+k\rangle)$ and $|e\rangle|m+k\rangle(|e\rangle|m\rangle)$, so $\Omega_{m,m+k} = \left|\Omega_{m,m+k}\right| e^{i\frac{k\pi}{2} - i\phi}$.

The $\hat{U}_k = \exp(-i\hat{H}_I^k t)$ notation denotes the temporal evolution operator. In order to discover the rule, we may broaden it and do the calculation $(\hat{H}_I^k)^2$, $(\hat{H}_I^k)^3$.

We are primarily interested in the interactions on the carrier ($k = 0$) and the first red (blue) sideband ($k = -1(+1)$) in terms of quantum coherent manipulations of a single ion. This is because these interactions are the fundamental components for the constructions of a wide class of quantum manipulations, such as sideband cooling and the spin-dependent force.

For $k = 0$

$$\begin{aligned} \hat{U}_c = & \sum_{m=0}^{\infty} \cos\left(\frac{\left|\Omega_{m,m}\right| t}{2} \right) (|g\rangle\langle g| \otimes |m\rangle\langle m| + |e\rangle\langle e| \otimes |m\rangle\langle m|) \\ & - i \sum_{m=0}^{\infty} \sin\left(\frac{\left|\Omega_{m,m}\right| t}{2} \right) \left(|e\rangle\langle g| \otimes |m\rangle\langle m| e^{-i\phi} + \text{ H.c. } \right) \end{aligned} \tag{2.38}$$

For $k = -1\,(+1)$

$$\begin{aligned} \hat{U}_{r(b)} = & \sum_{m=0}^{\infty} \cos\left(\frac{\left|\Omega_{m,m+1}\right| t}{2} \right) (|g(e)\rangle\langle g(e)| \otimes |m+1\rangle\langle m+1| + |e(g)\rangle\langle e(g)| \otimes |m\rangle\langle m|) \\ & - i \sum_{m=0}^{\infty} \sin\left(\frac{\left|\Omega_{m,m+1}\right| t}{2} \right) \left(|e\rangle\langle g| \otimes |m(m+1)\rangle\langle m+1(m)| e^{i\left(\frac{\pi}{2} - \phi\right)} + \text{ H.c. } \right) \\ & + |g(e)\rangle\langle g(e)| \otimes |0\rangle\langle 0| \end{aligned} \tag{2.39}$$

Even when the average phonon number of the motional state is rather large, the preceding forms may still be applied to the dynamics of the ions even while operating outside of the Lamb-Dicke regime. The majority of the time, especially after ground-state cooling of the ion motion, we only expand the Hamiltonian (2.33) to the first order of the Lamb-Dicke parameter η in the Lamb-Dicke regime. After doing so, the Hamiltonian (2.33) can be approximated to

$$\hat{H}_I = \frac{\Omega}{2}(\hat{\sigma}_+ e^{-i\delta t} + H.c.) + \frac{i\eta\Omega}{2}\left(\hat{\sigma}_+(\hat{a}^\dagger e^{i(\nu-\delta)t} + \hat{a}e^{-i(\nu+\delta)t}) + H.c.\right). \quad (2.40)$$

This is especially true after ground-state cooling of the ion motion. Setting δ close to 0, $-\nu$ and ν accordingly and disregarding the rather rapid rotating terms allows us to quickly get the carrier, the first red sideband, and the first blue sideband from this equation.

2.3.2 Raman coherent control

Consider now how the Raman laser beams would react if they were to contact with a single ion. This laser is called a pump laser and its frequency is ω_p and Rabi frequency Ω_p. The other laser is called a Stokes laser and its frequency is ω_s and Rabi frequency Ω_s. As we can see from Fig. 2.4, there are two laser beams coupling the spin-down state ($|\downarrow\rangle$) and the auxiliary state ($|1\rangle$). The laser-ion Hamiltonian under intraction picture is an extension of the equation that additionally considers the cross coupling terms (i.e. the pump (Stokes) beam also couples $|\uparrow(\downarrow)\rangle$ and $|1\rangle$), as well as the intraction picture.

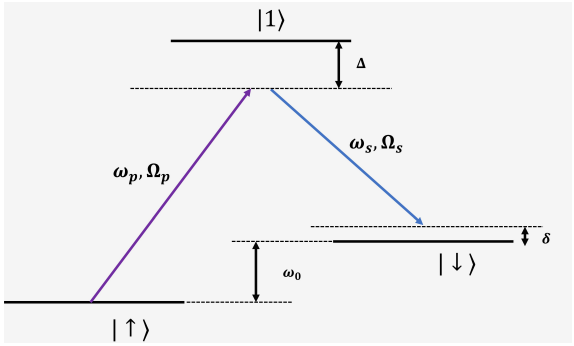

Figure 2.4 Level scheme of Raman transition.

2.4 notation

$^{171}\mathrm{Yb}^+$

$6^2P_{1/2}$

$|\downarrow\rangle$

$|\downarrow_z\rangle$

$|\uparrow\rangle$

CHAPTER 3 EXPERIMENTAL SETUP

3.1 Introduction

3.2 The Cryostat

The cryostat is the key equipment of the cryogenic trapped ion system. We need to pay attention to some key technical indicators when choosing the model of the cryostat, designing the internal support structure and the assembly structure of the trap-related components. The most critical technical indicators are cooling capacity and vibration. Low temperature is the advantage of the cryogenic trap over the room-temperature trap. We can achieve low pressure by cryo-pumping to reduce the collision rate of trapped ions with residual background gas, thereby increasing the lifetime of trapped ions. The price of cryo-pumping is additional vibration, however, the vibration can be reduced to a degree that does not affect Quantum Gate Fidelity. In experiments, we often use these two parameters to characterize the cooling capacity. One is the lowest temperature that the system can reach when the cryogenic trap is not temperature stabilized, and the other is the heating power at the sample stage when the temperature of the cryogenic trap is stabilized above the liquid helium temperature zone and the vibration caused by liquid helium is reduced to a certain range. Another key technical indicator of the cryostat is the long-term stability at the sample, including changes in displacement and background electric field. This will affect the calibration period of the ion trap experiment. Calibration that is too frequent indicates a lack of robustness in the experiment system. There are several different types of cryostats on the market. One of these is the flow cryostat, which has lower cryocooler vibration noise but requires constant replenishment of cold liquid coolant, which is expensive and time-consuming. In contrast, the cryogenic trapped ion system in our lab uses a closed-loop Gifford-McMahon cryostat. This type of cryostat uses closed-cycle helium gas as operation material in cooling cycle and does not require constant refilling of the coolant. It is very convenient to use and cheap to maintain as it only needs external electric supply. One of the advantages of this closed-loop cryostat is that it has a Vibration Isolation System (VIS). The vibrating cold finger is mechanically separated from the main vacuum by a helium-filled exchange gas region at a pressure 0.03 bar above atmospheric. The VIS is the only mechanical coupling between the cold head and the main vacuum apparatus which is mounted on an optical breadboard. In the VIS

region, it is sealed with a helium-confined rubber bellows. The helium gas serves as the thermal link between the cold finger and the sample stage where the ion trap is mounted. Another advantage of this closed-cycle cryostat is that its structure is relatively simple, and we can increase cooling capacity and reduce vibration through optimized design, because it is difficult to optimize each parameter independently in a complex system. The cryostat is model SHI-4XG-15-UHV, designed and manufactured by Janis Inc. In order to reduce vibration, we provide some design suggestions. The cryostat consists of a cold head, an exchange gas chamber and a vacuum chamber. The cold head is powered by a helium compressor. The models of cold head and helium compressor are RDK-415D2 and F70-H produced by Sumitomo Corporation of Japan. The cold head features two stages with different cooling powers: the 40 K stage has XX W, and the 4 K stage has XX W. The cold head must be fixed near the vacuum chamber, but there are only three interfaces of the cold head: the power supply, the supply high-pressure helium tube and the return high-pressure helium tube. Therefore, we placed the helium compressor and water cooler in the grey room of the laboratory to further isolate the source of vibration noise. The single continuous running time of the cold head can exceed 10,000 hours, which is enough for us to carry out long-term experiments. The exchange gas chamber is mainly composed of rubber bellow, helium pressure gauge and some helium valves, the top and bottom are respectively connected to the cold head and the vacuum chamber. The role of bellow is to reduce the vibration generated by the cold head and directly transmitted to the vacuum chamber, because rubber is more elastic than stainless steel. I think it is worth trying to replace the rubber bellow with a stainless-steel sheet that has been bent many times, because using a rubber bellow may cause leakage in the long-term operation of the system. Leakage of rubber bellow may come from three aspects. Firstly, the rubber material will deteriorate after a long-time use, our system has a leakage problem after about 2 years of operation, which is manifested as water inside the exchange gas chamber after the process of cooling down and warming up. Secondly, the rubber bellow is prone to defects during machining, we contacted our supplier to process a new rubber bellow after we found the leakage problem, and found that some of the rubber bellow had defects on the surface during many attempts. Finally, the sealing method of rubber bellow is worse than that of stainless steel, our cryostat uses o-ring to seal rubber bellow. We tried to have the supplier process different rubber bellow to test the leakage, such as testing different materials and thickness of rubber bellow, in some poor cases after a single cooling

and reheating process will appear leakage, we finally used silicone rubber bellow and the thickness is twice the original and no leakage has been found so far.

3.3 Low Temperature and UHV System

The vacuum chamber resembles a cylinder with a diameter of about XX and a height of about XX. Externally, the upper part of the vacuum chamber has some feedthroughs connecting the electrical equipment to the vacuum equipment, and the lower part is a spherical octagon. The top of the vacuum chamber is in contact with the exchange gas chamber, and the bottom is the re-entrant window. In our experiments, we used a total of three electrical feedthroughs, one DC feedthrough to drive the voltage signal to the electrodes of the trap, another DC feedthrough to drive the thermometer and heater in the vacuum chamber, and an RF feedthrough to drive the RF signal to the resonator. Below them, there are a total of three Vacuum feedthroughs, one connected to an ion gauge (Agilent UHV-24P) to monitor the vacuum level in the vacuum chamber, one connected to a NEG-Ion pump (SAES NextTorr Z100) to pump out hydrogen, since hydrogen is the least efficiently cryo-pumped gas, and an angle valve to pump out vacuum during system maintenance. A spherical octagon holds eight XX diameter windows to provide optical access in the horizontal plane, the windows are made of UVFS and have different wavelength optical coatings according to the optical path design. We replaced one of the windows along the trap axis with an oven feedthrough, and installed both enriched 171Yb oven and enriched 174Yb oven on it, and finally tested them to work. However, assembly errors during installation may cause the Yb flux cannot enter the trap during ion loading, we can increase the translation degrees of freedom when designing the part to solve this problem. According to our experience, because of the large divergence angle of Yb flux, we just need to be able to see the trap and oven through the opposite window. The re-entrant window located at the bottom of the vacuum chamber has a diameter of XX, below which is the imaging system. The maximum numerical aperture allowed for imaging ions along the vertical direction is XX. The Re-entrant window is surrounded by a cake-shaped aluminum base placed on an optical breadboard, and the base carries the full weight of the vacuum chamber. We tried to fasten between the upper part of the vacuum chamber and the optical breadboard with an aluminum sloped beam, but it did not reduce the vibration of the trap, indicating that the current support structure is solid enough. The main components inside the vacuum chamber are the 40K shield, the 4K

shield and the sample stage. These two shields are used to shield the ion trap from room temperature blackbody radiation, their material is aluminum, but copper may be a better choice because copper material has a higher thermal conductivity. The bottom of the two shields are eight 1" UVFS windows, which correspond to the spherical octagon and have the same optical coating. The glass is fixed in the groove by the Teflon holder in order to keep the windows from being crushed during the cooling procedure, however, because of the elasticity of Teflon, the positioning accuracy of the windows is poor, which may be the main source of optical aberration. The top of the 40K shield is in contact with the 40K stage of the cold head through the helium gas in the exchange gas chamber, which is usually higher than 40K, we named it that way just because it is intuitive. The top of the 4K shield is fixed to the sample stage, which is made of oxygen-free copper with a gold-plated surface to obtain a high thermal conductivity and to prevent oxidation during system maintenance. The sample stage and the 4K stage of the cold head are separated by a heat exchanger and cryogenic helium gas. The 4K stage can reach temperatures below 4K, and the heat exchanger is composed of a series of concentric circular oxygen-free copper sheets, which are designed to increase the cooling capacity at the sample stage. However, if the position between a pair of heat exchangers is shifted during operation and touches each other, it can introduce large vibrations to the sample stage, for example when floating the optical table. Although the cooling power of the 4K stage in the cold head reaches XX W, the cooling capacity of the sample stage in the vacuum chamber, which is directly available to the user, is much lower. The reduction of the cooling capacity comes from the heat conduction between the 4K stage and the sample stage and the heat leakage from the environment. In order to improve the heat transfer between the 4K stage and the sample stage, we can increase the surface area of the heat exchanger, we can also fill the exchange gas chamber with sufficient helium gas, and it is necessary to use oxygen-free copper to produce thermally conductive parts. In our experiments, we use auto gas charging system to stabilize the helium pressure in the exchange gas chamber at a fixed positive pressure. It is worth noting that the rubber bellow loses its vibration isolation function under negative pressure, and the life of the rubber bellow is reduced. The auto gas charging system was designed by PHYSIK and is based on the principle of using a PLC to read the helium pressure gauge and control the opening and closing moments of the helium valves, which will eventually stabilize the helium pressure gauge at 1.03 bar. There are two helium valves to control the helium inlet and outlet, and

one safety value to allow excess helium to escape, preventing the bellow from bursting when the auto gas charging system is not working. The temperature stabilize system is a kit we purchased from Janis Inc. and consists of a thermometer, heater and temperature controller. The thermometer (DT-670-CU-HT-1.4H) is located inside the sample stage in the vacuum chamber and has a measurement range of 1.4K-500K, covering the cryostat operating range of approximately 4K-300K. The heater is a 25 Ohm resistor very close to the thermometer. The DC lines of the heater and the thermometer are connected to the temperature controller (Model 26 from CryoCon) on the instrument rack via a DC feedthrough on the vacuum chamber. In low temperature operation, the temperature of the Sample Stage can be stabilized at 6K±XXmK for a long time by setting the appropriate PID parameters. The output power of the heater is about 350mW, which means that the cooling power of the sample stage has a margin of 350mW. The auto gas charging system and The temperature stabilize system are the key systems for the long-term stability of the cryostat. Although the temperature of This cryostat has almost no drift, we can observe that the trap can shift ±1 μm during the experiment. The operation to avoid the effects of such position shifts by frequent calibration of the system parameters is very complicated, so this instability can be fatal for an experimental system. The long drift of the sample stage comes from the mechanical structure of the cryostat. The auto gas charging system can only stabilize the helium pressure near the rubber bellow, and the 40K stage and 4K stage of the cold head are not stabilized. Therefore, the pressure and temperature in the contact part of the vacuum chamber and the exchange gas chamber cannot be stabilized for a long time. However, this part is the support point of the sample stage, so the sample stage will be disturbed by these external environmental changes. We can consider fixing the sample stage to the room temperature area of the vacuum chamber, which will not move if the laboratory environment is stable, but this will inevitably increase the heat leakage from the room temperature area. In our experiments, we first pumped the vacuum chamber to 1E-6 mBar at room temperature using the Turbo Pump, then activated the NEG-Ion Pump for about 2 hours, and at the end of the operation the vacuum chamber vacuum level dropped to 1E-8 mBar. The vacuum chamber can reach a vacuum level of 3E-10 mBar with the effect of the cryo-pump.

3.4 Helical Resonator and Segmented Blade Trap

The blade trap forms a capacitor of approximately XX pF. In order to drive this capacitor, i.e. to apply a high voltage signal to it, we need a larger helical resonator to form the LC oscillation circuit and to achieve impedance matching. The two components are therefore closely linked. The helical resonator and the blade trap are both located inside the 4K shield of the vacuum chamber. The helical resonator is fixed underneath the sample stage and then the blade trap is fixed underneath the helical resonator. This ensures that the helical resonator and the blade trap are very close to each other and that their temperatures are equally stable. At the same time the low temperature allows the resistance in the oscillator circuit to be significantly reduced, which helps to increase the Q factor of the oscillator circuit. The helical resonator and the blade trap are used as a single unit and its input and output are achieved via RF and DC electric feedthrough.

3.4.1 Design of Helical Resonator

The circuit models for the helical resonator and the blade trap have been well studied. In practice, we have developed a very mature design procedure with a high quality factor, choosing only two parameters □/□ and □/□ to optimise the performance of the helical resonator with the quality factor as the objective function. We can calculate the loading frequency in the empirical parameter regime using the trap capacitance and the quality factor. Typically, □/□ ≈ 1.5 and □/□ ≈ 0.5 is a good choice, and if the loading frequency meets our requirements we will try to choose the highest quality factor around this parameter range. A two-wire spiral resonator is much more complex than a single-wire spiral resonator because of the coupling between the two coils. However, for the sake of simplicity we are still using the model and we can achieve an accuracy of about ±5MHz. To ensure that the phase and amplitude of the two coils are the same, we use a parallel capacitor, which is shorted when connected to the RF feedthrough, with a capacitance of approximately 300 nF. The two-wire design is designed to help minimise micro-movements by applying a DC voltage to the RF electrodes, so we need to ensure that the RF signal on the coil is grounded and the DC voltage is not, this is achieved by a 300 nF capacitor connected to the shield. In addition, we added an RC filter before the DC voltage was connected to the coil.

3.4.2 Assembly of Helical Resonator

The material used for the body of the helical resonator is oxygen-free copper, which is characterised by its very low resistivity and high thermal conductivity. The low resistivity helps to obtain a high Q factor, but the oxygen-free copper is susceptible to oxidation during processing, so the oxide film needs to be removed before assembly. After the helical resonator has been assembled, it needs to be placed in a vacuum enclosure to prevent oxidation.

The main parts of the helical resonator were machined according to the design parameters: the antenna cover, the top cover, the middle part, the bottom cover and the helical coils, which were then cleaned in the ultrasound machine using acetone and ethanol. After drying these parts with nitrogen and soaking them in organic acid for 5 minutes, it can be observed that the surface oxide film disappears and turns purplish red. We soak the parts in plenty of distilled water to remove the residual organic acid and then dry the parts with nitrogen. The cleaning of the parts of the main part of the copper tube is now complete. This part needs to be done carefully, as the oxide film on the helical resonator surface affects the Q factor.

We also need to prepare and clean the rest of the parts according to the design parameters to meet the ultra-high vacuum requirements. We then soldered the circuit components together using lead-free solder. The parts are then assembled with stainless steel screws, each requiring a resilient pad to prevent the screws from loosening at low temperatures.

3.4.3 Assembly of Blade Trap

The advantage of the blade trap is that it is easy to process and assemble, but the disadvantage is that the assembly error is higher compared to the surface trap or the monolithic trap, which causes an asymmetry in the electrostatic potential at the centre of the trap where the ions are located, i.e. a deviation from the linear trap configuration. When designing the blade trap for use in the cryostat, we need to take care that the material has a high thermal conductivity and that the connections between the components are sufficiently tight. In this way we can achieve the lowest temperatures on the blade trap. This helps to obtain a higher vacuum level and to extend the life of the ions.

The blade trap consists of four blade-shaped electrodes, one pair of DC electrodes and one pair of RF electrodes. The blade is processed by laser cutting the ceramic substrate and then plating the surface with a gold layer. The electrodes are machined with a certain

amount of error and defects on the surface of the electrode closest to the ion produce a high level of electrical noise, which can be reduced by improving the process. We have machined a sapphire adapter plate and mounted the blade on the sapphire adapter plate and then mounted the sapphire adapter plate on an oxygen-free copper holder. We designed this adapter to avoid a short circuit between the blade and the ground (the blade holder). In order to increase the thermal conductivity, we need to cover these contact surfaces with indium foil. For the fixing of the components we used stainless steel screws and used resilient pads on each screw. This is to prevent the screws from loosening during the cooling down process, and to prevent the blade from being crushed by excessive torque when tightening the screws. Once installed we had to fine-tune the position of the sapphire adapter under the microscope to keep the assembly error small enough. This operation makes use of the fact that the diameter of the through-hole is slightly larger than the diameter of the screw. Since the assembly is done by hand, this part of the assembly error is unavoidable.

The connection of the blade electrodes is mainly done by means of gold ribbon (AMETEK) and Kapton insulated wire (Accu-Glass Products). When selecting materials we need to be aware of ultra-high vacuum and cryogenic compatibility. Some of the circuit connections are made prior to assembly and the rest is done afterwards. Before assembling the blade, a 820pF capacitor is fixed with silver epoxy between each DC electrode and ground on the two DC blades. The purpose of this capacitor is to create a low impedance between the DC electrodes and ground, reducing the voltage splitting of the RF signal on the DC electrodes. The gold ribbon is connected to the electrodes with the spot welder at one end and to the pads of the PCB with solder at the other. We will later connect the pads to the corresponding connections with Kapton insulated wire, where the DC electrode wires are connected to the corresponding wires from the DC feedthrough through the heat sink twice, and the two RF electrode wires are connected to the two wires at the output of the helical resonator.

3.5 Yb Oven

In order to generate the atomic beams of Yb, we built two separate ovens from two stainless steel tubes, but integrated into a single feedthrough and both able to be used to load ions. The 171Yb oven has an abundance of 90% and The 174Yb oven has an abundance of 98%. As the Yb source is in block form, we need to cut it into small pieces

and insert it into the stainless steel tube.

In order to achieve UHV compatibility we chose to use copper, stainless steel and Macor when machining the parts of the oven. Before assembly and testing, we cleaned all the parts inside the ultrasound machine using acetone and ethanol as solvents. All the parts were assembled according to the drawings and the copper wires on the feedthrough were attached to the stainless steel base, which was all screwed in place. We then used a spot welder and welded the stainless steel tube to the stainless steel wire, and the stainless steel wire to the stainless steel base, respectively. As the stainless steel tube has the smallest cross-sectional area, the highest resistance in the whole circuit is at the stainless steel tube, about 0.5 Ohm, so the temperature is highest here too. I would recommend having some extra spare parts and testing the parameters of the spot welder in advance, as the stainless steel tube can easily break under unsuitable parameters. Finally the two Yb sources are filled into the corresponding stainless steel tubes.

Each oven is mounted in such a way that the outgoing atomic beam is directed towards the trapping area. The oven feedthrough replaces an XX inch window in the axial direction of the trap. the glass in the corresponding position of the 40K shield and 4K shield is also replaced with a round aluminium plate, the centre of which is a square hole with a 5mm side to pass through the Yb flux. As the cryostat has assembly errors, I would recommend preparing round aluminium plates with different opening positions in advance. Ultimately we need to be able to see the trap through the opposite window, with the square hole and the oven in the same line.

In the process of loading ions, when this stainless steel tube is heated resistively by an electric current, a spray of atomic Yb is produced. The temperature reached depends on the current and the time of operation. If either of these two factors is too high or too long, this can lead to rapid evaporation of the Yb and thus the formation of a spray dense enough to cover its surface (e.g. ion trap electrodes or vacuum windows). To prevent this, each oven is tested in advance. A stainless steel sheet is placed in front of the oven and then the oven is placed in a transparent vacuum chamber and the vacuum is reduced to approximately 4E-6 mbar using a turbo-molecular pump, so that a test system can be set up. We tested each oven in turn, starting at 0 A and increasing the current by 0.1 A every 10 seconds, observing the change in vacuum level and the colour of the stainless steel sheet. We can observe both the darkening of the stainless steel sheet and the rapid rise in pressure, at which point the current value is the threshold current for the corresponding

oven. 171Yb oven has a threshold current of 4.2A and 174Yb oven has a threshold current of 3.9A, but the current values we use in practice will be lower than this threshold, the exact values need to be measured in the corresponding experiments. The exact values need to be measured in corresponding experiments, such as observing the fluorescence of Yb atoms and loading Yb ion.

3.6 Mechanics Frame

3.7 Optical and Imaging System

Whether trapping ions or manipulating them, we need lasers. In our laboratory, tunable diode lasers (Toptica) are used widely, mainly because these products are very well mature. For ion trap systems, a stable light source is very important. Experimentally, we need these lasers to be switched on and off quickly, typically in a few hundred nanoseconds. It is also necessary that these lasers can be stabilised over long periods of time and that these laser controllers have stable software systems. Laser stabilisation covers mode, frequency, power and polarisation. Typical laser stabilisation lasts from a few hours to a day, including laser frequency locking. This is sufficient for our trapped ion experiments, but longer stabilisation times are preferable. In the experiments, these stable lasers are used for: ion loading, Doppler cooling, optical pumping, state detection, repumping and sympathetic cooling. In addition to the laser light path into the cavity, I also built an imaging system to collect the fluorescence emitted by the ions, enabling real-time observation and state detection of the ions.

3.7.1 Laser Sources and Power Allocation

The light sources in the laboratory are placed on several separate optical tables. Since the principles of the optical path setup are similar, we can present the light sources and power allocation in a common way. The cryogenic trap platform requires a 370nm laser, a 399nm laser and two 935nm lasers. The two 935 nm lasers are shared with other ion trap platforms in the lab, one for trapping 171Yb+ ions and the other for trapping 174Yb+ ions. The 399nm laser is used for loading ions. Depending on the type of ion to be loaded, 171Yb+ or 174Yb+, we can change the wavelength of the 399nm laser. This 399nm laser is also shared with other trapped ion platforms in the lab and only one 399nm laser is needed. Since loading ions is not very frequent and most of the time we need to load 171Yb+ ions, and modifying the wavelength of the 399nm laser will not affect the stable

trapping of the loaded ions.

The output power of a semiconductor laser is approximately XXmW, depending on the wavelength and model, the laser output power may vary a little. The output power of the 370nm laser (L1) is XXmW, the output power of the 399nm laser (L2) is XXmW, the output power of the 935nm laser (L3) is XXmW and the output power of the 935nm laser (L4) is XXmW.

As the nominal light output from the laser is linearly polarised, a power attenuation unit was formed using a half-wave plate（HWP）and polarization beam splitter（PBS ）to split the laser output into two parts, which are separately coupled into the fibre. Each fibre will act as the light source for the next stage of the optical path, thus making the optical path a modular one. Each laser has one optical fibre connected to the wavemeter (C5, C6, C7, C8). Because polarisation stabilisation is not required, a single-mode fibre is used, with a typical power of approximately 50 μW. The other fibres are the light sources for the rear optical paths (C1, C2, C3, C4) and require high power, typically 5 mW. At the same time their polarisation needs to be stable over time and we use single-mode polarization-maintaining fibres. In order to adjust the polarisation direction to match that of the single-mode polarisation-maintaining fibre, we use a polarisation adjustment unit consisting of a HWP and quarter-wave plate（QWP）. We need to maximize the efficiency of the fiber coupling, which requires a good laser output mode and good mode matching, which can be done with a lens pair, I don’t show this in the diagram.

The 370nm laser also has two splits: one (C9) is connected to the optical cavity for narrow linewidth frequency locking of the laser, and the other (C10) is set aside. 171Yb+ repumping beam requires XX sidebands, so the 935nm laser (L3) has a fibre EOM (E1) in the rear optical path.

3.7.2 Laser Frequency Stabilization

The target linewidth of the laser frequency locking determines the laser frequency locking scheme. In my experiments there is no need for ultra-narrow linewidth laser locking, so the laser locking scheme is relatively simple and I have mainly optimised the automatic control of the frequency locking process. The measurement and locking of the laser frequency can be achieved with a wavelength meter, which has a relatively low bandwidth of about 10 Hz because the sum of the measurement time of the multi-channel wavelength meter and the computer readout time is about 100 ms. The standard deviation of the output frequency of the laser locked with this scheme is about 1MHz,

which meets my needs with a 399nm laser and two 935nm lasers, or if only to trap a small amount of ions then also my requirements for a 370nm laser. The outgoing light from the laser is transmitted by optical fibres (C5, C6, C7, C8) to the input of the wavemeter, which is programmed to read the frequency on our PC and then programmed to adjust the voltage signal from the laser controller, thus creating a closed loop that locks the laser frequency. The wavemeter's measurements are affected by the environment, mainly air pressure and temperature. Therefore this frequency locking scheme will cause the locked laser frequency to be inaccurate due to inaccurate measurements, but this error is slow and periodic over time. So for 399nm laser and 935nm lasers we don't take this into account. I only calibrate the 370nm laser once in 1 hour or longer, by measuring the resonant frequency of the Yb+ ion and feeding it back to the wavemeter's lock point. It would be possible to automatically calibrate the wavemeter for measurement errors if the wavemeter had a locked reference light all the way through, such as a 780nm laser, but we have not done this because it is not necessary. The implementation of an automatic frequency lock is necessary as it will simplify the steps of daily operation. By laboratory standards these lasers need to be switched off when they are not in use, for example every night. I will adjust the operating parameters of the laser so that the laser mode can be stabilised back to a specific frequency range for approximately 10 minutes after each switch-on operation, which requires us to find a stable operating parameter for the laser. We then only need to program to communicate with the laser and the wavemeter to achieve automatic laser control and frequency locking.

The results of targeting the 370nm laser with a wavemeter are not good enough because the feedback speed is too slow. We can increase the feedback speed with the assistance of an optical cavity, which reduces the standard deviation of the output frequency of the 370 nm laser to 300 kHz. I built this optical path on a breadboard in which an optical cavity (U2; SA200-3B, Thorlabs) was placed. The outgoing light from the 370 nm laser (C9) is incident to the optical cavity. mode matching of the optical cavity is achieved by a pair of reflectors and lenses. Locking the 370nm laser to the optical cavity is achieved by feeding the output signal of the photodiode (D1) back to the voltage signal of the 370nm laser controller. In order to have the lock point at the point of maximum transmission light intensity of the optical cavity, I added a modulation signal to the current signal of the 370nm laser and demodulated the signal from the photodiode (D1). This solution uses a simple optical cavity to increase the bandwidth of the laser locking. This scheme

uses a simple optical cavity to increase the bandwidth of the laser locking. However, because environmental factors can cause the cavity length of the optical cavity to change, the locked frequency will change rapidly as the cavity length changes. I connected the voltage signal (S1) from the wavemeter output to the piezoelectric ceramic (P1) of the optical cavity, thus achieving a locking of the optical cavity length to the wavemeter.

3.7.3 Laser Modulation

Making the laser modulation a separate module allows for modularisation of the optical path, which facilitates maintenance and testing, and also reduces the size of the optical path into the cavity, which in turn reduces the area of the breadboard where the cryogenic trap vacuum chamber is located. The main source of laser leakage during laser modulation is the higher order modes of the laser and stray light from the crystal during modulation. Adding a stage of fibre coupling can act as a spatial filter and help reduce leakage.

Experimentally, I need to add sidebands to the 370nm laser, the 14.7GHz sideband (E2) for Doppler cooling and the 2.105GHz sideband (E3) for optical pumping. the electro-optic modulator（EOM）can implement these features. The frequency and modulation depth of the sidebands can be controlled by controlling the frequency and amplitude of the EOM input microwave signal. In addition, I need to control the frequency shift and power of the 370nm laser. This is because the difference in frequency required for Doppler cooling and state detection is approximately 12MHz, and the frequency variation measured during calibration of the system can be compensated for by adjusting the frequency shift of the 370nm laser. The acousto-optic modulator（AOM）provides these features. By controlling the frequency and amplitude of the microwave signal input to the AOM（A1）the frequency of the laser shift and the laser power can be controlled.

The light source from the 370nm laser is fed to the laser modulation module via a single-mode polarization-maintaining fibre (C1), which is reflected by a beam sampling mirror and enters the laser monitoring module (U3). A number of signal acquisition modules are integrated into the laser monitoring module to help me monitor the quality of the light source over time, including measurements of power , polarisation, laser mode and others. The main light source is modulated by two cascaded EOMs, the modulation depth of which can be maximised by adjusting the HWP. Part of the laser is coupled into the fibre (C12), which is then used for sympathetic cooling. To achieve the frequency shift, I built a double-pass configuration based on a 4f optical system, where the PBS serves to separate the incident light from the returned light by 90°, adjusting the HWP at the front

to maximise the efficiency of the incident light and the HWP at the back to maximise the efficiency of the diffraction from the AOM. When the laser passes through the AOM, 0 order light is discarded and +1 order light is returned to the AOM by a 4f optical system consisting of a lens and a D-shaped pickoff mirror. The +1 order beam from the reflected beam passes through the QWP twice and is then reflected by the PBS into the fibre (C11), this light is then used for global cooling, pumping and detection. There is a mechanical shutter（N1）in front of the fibre, which serves to completely shut off the light and reduce leakage.

3.7.4 Optical Layout of Cryostat Breadboard

Due to the large base area of the cryostat, the area left for the optical path on the breadboard is relatively small. the main function of the optical path built on the breadboard of the cryostat is to shape the beam into a specific shape and then inject it into the cavity. There are four windows on the Cryostat that are used to inject the laser. The laser light exiting the fibre collimator (C2, C3, C4, C11, C12) is first polarised by the QWP and HWP and then expanded by the lens pairs (T1, T2, T3, T4) to a suitable spot size, typically with a Gaussian diameter of approximately 10 mm. It is then incident on a long-focus lens (L1, L3, L5, L7) into the cavity and forms a small spot in the centre of the trap, typically with a Gaussian diameter of about 20 μm. The long-focus lenses are mounted on a 3-axis linear stage (G1, G2, G3, G4； M-461-XYZ-M, Newport) with a Picomotor actuator (8301NF, Newport) in each axis of the stage to achieve high precision control of the beam position. Reducing the spot diameter at the trap is necessary to increase the power density, reduce stray light and improve the signal to noise ratio. It also helps me to monitor the displacement of the spot relative to the ions over time, which helps me to find unstable components or modules in the system at the beginning of the construction of the system. But when the length of the ion chain in the trap increases, I need some light spots to expand in the horizontal direction to about 500 μm in diameter. It is advantageous to be able to easily adjust the spot diameter in the horizontal direction. I added cylindrical lenses (L2, L4, L6) to the optical path where I needed to adjust the horizontal diameter, and by artificially introducing astigmatism, I was able to shift the horizontal focal position along the optical axis. A long-focused cylindrical lens with a focal length of approximately 1000 mm is generally used, mounted on a rotatable lens mount so that the tilt angle of the elliptical spot can be adjusted and the cylindrical lens can be removed when the elliptical spot is not required.

The stability of the 370nm laser (C11) is so important to the experiment that a laser monitoring module (U4) has been installed at the outgoing point of the fiber. This light is global light and is required for ion loading, Doppler cooling, optical pumping, and state detection. In order to trap both 171Yb+ and 174Yb+, two 935nm lasers (C3 and C4) were combined into the cavity and their function was rupumping. Combining these two 935nm lasers at the front stage would have been a better option, but this was not done due to space planning in the laboratory. The 399nm laser (C2) is used for ion loading and the 370nm laser (C12) is used for sympathetic cooling.

A permanent magnet is placed in front of one window to generate a magnetic field at the centre of the trap, approximately XX Gauss, perpendicular to the direction of the ion chain. A horn is placed in front of one of the windows to apply microwaves.

3.8 Electronic Devices

CHAPTER 4 EXPERIMENTAL PROCEDURE

4.1 Start CryoServer

4.2 Cooling-down and warm-up

The cryogenic trapped-ion system is a relatively complex experimental system, and we need the system to be stable over a long period of time so that the reproducibility of the measurement results is high. Although the cryostat's core component, the cold head, can run continuously for more than XX hours, the maximum time this cryostat can run continuously is limited by the stability of the power supply, the stability of the laboratory temperature and humidity, and whether the exchange gas chamber is leaking. It took us about three years to get the system into a stable long-term state, after which we conducted a series of physical experiments on the experimental platform. However, during the three-year commissioning process, we inevitably need to conduct the cycle of cooling-down, malfunction, warm-up, and upgrade, during which the standardized operation helps to make the physical parameters of the system more repeatable, so we have developed a standardized operation procedure for this system.

4.2.1 Maintenance of the exchange gas chamber

If the cold head does not need to be removed for servicing, the exchange gas chamber does not require frequent maintenance and is always in an independent and stable state, whether it is being cooled down or warmed up.

The exchange gas chamber uses helium gas with a purity of XX. When we expose the exchange gas chamber to atmosphere or when it is first used, the internal gas needs to be purified. According to the cryostat manufacturer's recommendations, a purification is also required after several months of continuous running, but this is not normally done when the system is stable for a long period of time. How often the exchange gas chamber needs to be purified depends on the rate of impurity gases (nitrogen, oxygen, water vapour etc.) leaking in from the atmosphere.

When we need to purify the helium gas in the exchange gas chamber, the exchange gas chamber is first evacuated continuously for 0.5 hours with a dry scroll pump (Agilent IDP-7), then the valve connected to the dry scroll pump is closed and the valve connected to the helium gas is opened. The auto gas charging system will then raise the pressure to

1.03 bar and finally we close the valve to the helium gas. In general, the above operation is repeated three times to purify the helium gas in the exchange gas chamber.

When we need to cool down or warm up the system, and also when the system is running at low temperatures for a long time, we simply open the valve to the helium gas and keep the auto gas charging system running steadily.

4.2.2 Cooling-down

In the Cooling-down procedure, the physical parameters of the vacuum chamber are mainly adjusted and observed. The vacuum chamber is first connected to a turbo-molecular pump (TPS-compact Turbo Pumping System) via the angle valve and after approximately 48 hours of continuous operation the vacuum chamber reaches a vacuum level close to UHV. The ion gauge is switched on and reaches an indication of 5E-8 mBar, at which point we do not need to degas the ion gauge as the room temperature zone of the vacuum chamber does not eventually fall below 1E-10 mbar. Now we need to perform a time limited activation of the NEG Pump for 1 hour, then we perform several degas of the Ion Pump and keep the Ion Pump on. Now that the activation of the NEG-Ion Pump is complete, we close the angle valve and wait about 1 hour for the ion gauge to gradually decrease to 3E-9 mbar, when the vacuum chamber reaches the UHV vacuum level. We turn on the cold head and the temperature stabilize system, which will finish cooling down within 5 hours, but the system will not reach final stabilization for more than 24 hours. The temperature of the 4K stage is finally stabilised at 6K and the ion gauge is stabilised at 3E-10mbar.

4.2.3 Warm-up

The warm-up procedure is much easier than the cooling-down procedure because we do not need to obtain UHV during this process. we turn off the cryogenic and vacuum related instruments: the NEG-Ion pump, the ion gauge, the cold head. We can use the heater in the temperature stabilize system to heat the cryostat to speed up the warming process to room temperature, which takes about 24 hours or more. The system can also be allowed to warm up naturally to room temperature, which takes about 48 hours or more. Next, if necessary, we can move the cryostat into the service area for servicing. Before moving it out, we need to record the readings of all optical and electrical instruments. As the imaging system is embedded in the re-entrant window, we usually need to remove the objective lens.

REFERENCES

APPENDIX A 补充内容

附录是与论文内容密切相关、但编入正文又影响整篇论文编排的条理和逻辑性的资料，例如某些重要的数据表格、计算程序、统计表等，是论文主体的补充内容，可根据需要设置。

A.1 图表示例

A.1.1 图

附录中的图片示例（图 A.1）。

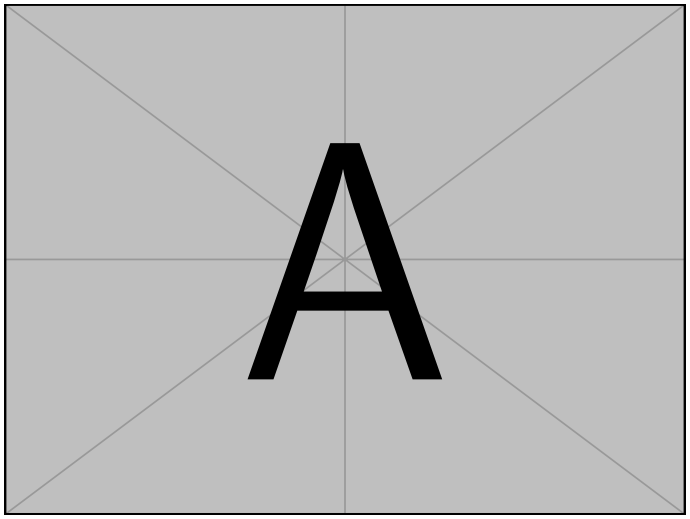

Figure A.1　附录中的图片示例

A.1.2 表格

附录中的表格示例（表 A.1）。

Table A.1　附录中的表格示例

文件名	描述
thuthesis.dtx	模板的源文件，包括文档和注释
thuthesis.cls	模板文件
thuthesis-*.bst	BibTeX 参考文献表样式文件
thuthesis-*.bbx	BibLaTeX 参考文献表样式文件
thuthesis-*.cbx	BibLaTeX 引用样式文件

A.2 数学公式

附录中的数学公式示例（公式 (A.1)）。

$$\frac{1}{2\pi \mathrm{i}} \int_{\gamma} f = \sum_{k=1}^{m} n(\gamma; a_k) \mathscr{R}(f; a_k) \tag{A.1}$$

ACKNOWLEDGEMENTS

衷心感谢导师 ××× 教授和物理系 ×× 副教授对本人的精心指导。他们的言传身教将使我终生受益。

在美国麻省理工学院化学系进行九个月的合作研究期间，承蒙 Robert Field 教授热心指导与帮助，不胜感激。

感谢 ××××× 实验室主任 ××× 教授，以及实验室全体老师和同窗们学的热情帮助和支持！

本课题承蒙国家自然科学基金资助，特此致谢。

声　明

本人郑重声明：所呈交的学位论文，是本人在导师指导下，独立进行研究工作所取得的成果。尽我所知，除文中已经注明引用的内容外，本学位论文的研究成果不包含任何他人享有著作权的内容。对本论文所涉及的研究工作做出贡献的其他个人和集体，均已在文中以明确方式标明。

签　名：_____ 日　期：_____

RESUME

个人简历

197× 年 ×× 月 ×× 日出生于四川 ×× 县。

1992 年 9 月考入 ×× 大学化学系 ×× 化学专业，1996 年 7 月本科毕业并获得理学学士学位。

1996 年 9 月免试进入清华大学化学系攻读 ×× 化学博士至今。

在学期间完成的相关学术成果

学术论文

[1] Yang Y, Ren T L, Zhang L T, et al. Miniature microphone with silicon-based ferroelectric thin films[J]. Integrated Ferroelectrics, 2003, 52:229-235.

[2] 杨轶, 张宁欣, 任天令, 等. 硅基铁电微声学器件中薄膜残余应力的研究 [J]. 中国机械工程, 2005, 16(14):1289-1291.

[3] 杨轶, 张宁欣, 任天令, 等. 集成铁电器件中的关键工艺研究 [J]. 仪器仪表学报, 2003, 24(S4):192-193.

[4] Yang Y, Ren T L, Zhu Y P, et al. PMUTs for handwriting recognition. In press[J]. (已被 Integrated Ferroelectrics 录用)

专利

[1] 任天令, 杨轶, 朱一平, 等. 硅基铁电微声学传感器畴极化区域控制和电极连接的方法: 中国, CN1602118A[P]. 2005-03-30.

[2] Ren T L, Yang Y, Zhu Y P, et al. Piezoelectric micro acoustic sensor based on ferroelectric materials: USA, No.11/215, 102[P]. (美国发明专利申请号.)

COMMENTS FROM THESIS SUPERVISOR

论文提出了……

RESOLUTION OF THESIS DEFENSE COMMITTEE

论文提出了……

论文取得的主要创新性成果包括：

1. ……

2. ……

3. ……

论文工作表明作者在 ××××× 具有 ××××× 知识，具有 ×××× 能力，论文 ××××，答辩 ××××。

答辩委员会表决，（× 票/一致）同意通过论文答辩，并建议授予 ×××（姓名）×××（门类）学博士/硕士学位。